


## Article

# Preparation of Oxygen Reduction Catalyst Electrodes by Electrochemical Acidification and Synergistic Electrodeposition

Liheng Zhou , Yongjian Guo, Yu Xu, Ping Li  and Qi Zhang \*

State Key Laboratory of Chemical Engineering, East China University of Science and Technology, Shanghai 200237, China; y30210137@mail.ecust.edu.cn (L.Z.); y30220095@mail.ecust.edu.cn (Y.G.); y82200081@mail.ecust.edu.cn (Y.X.)

\* Correspondence: lipingunilab@ecust.edu.cn (P.L.); zhangqi@ecust.edu.cn (Q.Z.)

**Abstract:** A proton exchange membrane fuel cell (PEMFC) is an efficient and environmentally friendly power production technology that uses hydrogen energy. The cathodic oxygen reduction electrode is a critical component in the development of PEMFC. Most techniques deposit catalyst nanoparticles in areas that are inaccessible for catalytic processes, reducing platinum utilization. The substrate used in this study was carbon paper (CP) with a self-supporting structure. First, electrochemical acidification technology was employed to modify the CP's surface, followed by nanoparticle manufacturing and fixation on the CP in a single step by electrodeposition. The Pt/C<sub>0.5</sub>V<sub>2.24</sub>CP catalyst electrode demonstrated high-quality activity in the oxygen reduction reaction (ORR), with a homogeneous particle dispersion and particle size of around 50 nm. The mass activity and electrochemical active surface area (ECSA) of the Pt/C<sub>0.5</sub>V<sub>2.24</sub>CP catalyst electrode were 1.74 and 3.98 times higher than those of the Pt/C/CP-1 electrodes made with commercial catalysts, respectively. After 5000 cycles of accelerated durability testing (ADT), the mass activity and ECSA were 1.28 times and 6.16 times more than Pt/C/CP-1. This paper successfully proved the viability of electrodepositing Pt nanoparticles on CP following acidification, and that the electrochemical acidification methods have a positive influence on improving electrode ORR activity.

**Keywords:** fuel cell; oxygen reduction reaction; electrodeposition; catalyst electrode



**Citation:** Zhou, L.; Guo, Y.; Xu, Y.; Li, P.; Zhang, Q. Preparation of Oxygen Reduction Catalyst Electrodes by Electrochemical Acidification and Synergistic Electrodeposition. *Catalysts* **2024**, *14*, 300. <https://doi.org/10.3390/catal14050300>

Academic Editor: Maria Victoria Martínez Huerta

Received: 4 April 2024

Revised: 22 April 2024

Accepted: 30 April 2024

Published: 2 May 2024



**Copyright:** © 2024 by the authors. Licensee MDPI, Basel, Switzerland. This article is an open access article distributed under the terms and conditions of the Creative Commons Attribution (CC BY) license (<https://creativecommons.org/licenses/by/4.0/>).

## 1. Introduction

Fuel cells are largely regarded as the best power sources for hydrogen utilization to date. Proton exchange membrane fuel cells (PEMFC) with operating temperatures below 100 °C have gained popularity due to their high technical maturity and commercialization compared to other fuel cell types [1]. Among the many challenges faced by fuel cells, the synthesis route of the cathodic oxygen reduction catalyst electrode is an important factor affecting the cell. At the same time, the traditional synthesis route increases the production cost of electrodes. In the traditional synthesis route, the catalyst nanoparticle (NP) is synthesized on the carbon carrier, mixed with the binder and polymer to make the electrocatalyst ink, and then sprayed on the gas diffusion layer (GDL) [2,3]. However, the catalyst NPs in this method show a low utilization of oxygen reduction activity, due to poor contact with catalyst NPs, electrolytes, and oxygen [4,5].

Directly electrodepositing catalyst NPs onto the GDL ensures that metal ions occupy the highest position in the local electric field, with a short path and a high local charge density, hence increasing platinum usage efficiency [6]. In addition, electrodeposition can simplify the manufacturing process of catalytic electrodes by reducing the required process steps for catalyst synthesis, thereby reducing production costs. A step voltage of −0.25 (or 0 V) to 0.85 V (vs. SCE) was used by Lüsi M et al. [7] to electrochemically deposit Pd on various nanocarbon substrates. There is more activity in the Pd/C catalysts that are placed on the GNS and CNT-GNP. Kim Y et al. [8] directly electrodeposited Cu onto carbon paper (CP), a microporous material, using hydrogen bubbles as templates. They

subsequently loaded Pt onto the CP via a straightforward displacement process. Following accelerated durability testing (ADT), the catalyst's current density is  $0.79 \text{ A} \cdot \text{cm}^{-2}$ , or 96.1% of its initial value of  $0.82 \text{ A} \cdot \text{cm}^{-2}$ . Following ADT, the maximum power density reduced slightly, from  $0.58 \text{ W} \cdot \text{cm}^{-2}$  to  $0.56 \text{ W} \cdot \text{cm}^{-2}$ , retaining 95.9% of the initial value and exhibiting remarkable resilience. Using polystyrene spheres of varying sizes as templates, Liu Y-R et al. [9] coated the spheres on CP using a multi-layer spin coating technique. Atomic layer deposition (ALD) technology was then utilized to produce titanium dioxide ( $\text{TiO}_2$ ) thin films on the template. After directly nitriding  $\text{TiO}_2$  in a flowing ammonia environment over  $800^\circ\text{C}$ , platinum nanoparticles were uniformly deposited on TiN via ALD, resulting in the formation of the TiN inverse opal structure. When compared to commercial E-Tek, its catalytic performance was 13 times greater in terms of platinum specific power density. Even though electrodeposition produces larger nanoparticles than chemical methods, electrodeposition produces nanoparticles with unique structures such as petal-shaped [10,11], granular [12,13], dendritic [12,14], polyhedral [15,16], spike-like structures [17,18], and more active sites, which enhances their electrocatalytic activity compared to commercial catalysts.

CP has a high and easily accessible exposed surface, which can shorten the oxygen diffusion path and promote rapid reaction kinetics. In addition, CP has a porous structure that can provide enough sites for oxidation and reduction reactions, as well as high conductivity and isotropic conductivity [19,20]. It is challenging to deposit valuable metals on the surface of CP due to its high degree of graphitization, reduced defect count, and increased hydrophobicity. To overcome its flaws, such as inadequate surface functionalization, low active specific surface area, and low hydrophilicity, CP must be modified. Liu et al. [21] improved the surface morphology, functional groups, and degree of surface defects of CP by electrochemically treating it in three solutions ( $\text{Na}_2\text{SO}_4$ ,  $\text{NaOH}$ , and  $\text{H}_2\text{SO}_4$ ). The membraneless microfluidic fuel cell (MFC) treated in  $\text{H}_2\text{SO}_4$  solution achieved the best performance, with a volume power density of  $235.6 \text{ mW} \cdot \text{cm}^{-3}$  and a volume limit current density of  $1063.33 \text{ mA} \cdot \text{cm}^{-3}$ , which were 1.58 times and 1.52 times higher than the untreated MFC, respectively. This optimal performance can be attributed to the activated CP in the  $\text{H}_2\text{SO}_4$  solution having the most oxygen-containing functional groups, the largest electrochemical active surface area, the strongest iron ion reduction, and the smallest resistance. Zhu W et al. [22] heated the CP in an alkaline environment and sonicated for 30 min, then activated the surface activity of the CP by cyclic voltammetry in a 4 M  $\text{HNO}_3$  solution. The catalyst exhibited excellent reactivity for the reduction of concentrated  $\text{HNO}_3$ , mainly due to the introduction of defects and heteroatoms into the surface of carbon fibers during the acidification process, which improves the surface wettability and enhances the activity of the catalyst.

In this work, oxygen reduction catalyst electrodes were prepared by a novel method of electrochemical acidification combined with electrodeposition. Firstly, methodologies and characterization techniques such as optical photos, scanning electron microscopy (SEM), Fourier transform infrared (FTIR), X-ray photoelectron spectroscopy (XPS), X-ray diffraction detection (XRD), and Raman were used to assess the oxygen-containing groups and surface structure of CP. Secondly, the effects of oxygen-containing functional groups on the surface of catalyst electrodes and the valence state of platinum were studied by XPS. Then, XRD and transmission electron microscopy (TEM) methods were used to search for the effects of the carbon and platinum crystal planes. SEM was used to observe the morphological differences of platinum NPs. Finally, the electrode was selected for half-cell testing by cyclic voltammetry (CV) measurements and linear sweep voltammetry (LSV) measurements. The performance of the catalyst electrode was evaluated using the electrochemical active surface area (ECSA), onset potential, and Tafel slope before and after durability evaluation.

## 2. Results and Discussion

### 2.1. CP Treated under Different Acidification Concentrations and Voltages

Figure 1a–d show photos of CP samples treated with different acidification voltages. It could be clearly observed that after applying the acidification voltage, the color of the CP changed from gray to a distinct dark black. This was a distinctive feature of the oxidized CP surface [23]. As the voltage increased, the surface color of CP darkened, and the oxidation effect of carbon fibers increased. From Figure S1 and Table 1, it could be seen that after applying a 2.24 V voltage, the surface C/O ratio of CP turns from 85.21 to 5.23. This confirms that electrochemical acidification could quickly and effectively improve the surface oxidation degree of CP.

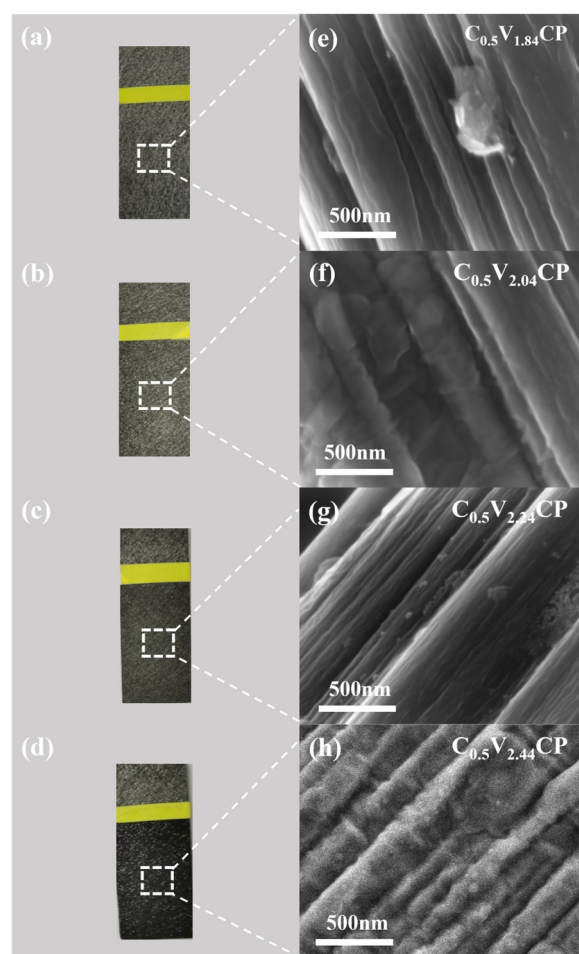


**Figure 1.** (a–d) Photo images and (e–h) scanning electron microscopy (SEM) images of the  $C_{0.5}V_{1.84}CP$ ,  $C_{0.5}V_{2.04}CP$ ,  $C_{0.5}V_{2.24}CP$  and  $C_{0.5}V_{2.44}CP$  samples.

**Table 1.** Summary of X-ray photoelectron spectroscopy (XPS) data of different catalysts.

Substrate	C:O	Catalyst	C:O	Pt Wt%	Pt <sup>0</sup> :Pt <sup>2+</sup>	Pt <sup>0</sup> :Pt <sup>δ+</sup>
$C_{0.5}V_{0.24}CP$	85.23	Pt/ $C_{0.5}V_{0.24}CP$	7.87	84.78	2.25	2.25
$C_{0.5}V_{1.84}CP$	2.29	Pt/ $C_{0.5}V_{1.84}CP$	8.34	80.45	2.24	2.24
$C_{0.5}V_{2.04}CP$	4.63	Pt/ $C_{0.5}V_{2.04}CP$	8.65	67.62	2.07	2.07
$C_{0.5}V_{2.24}CP$	5.31	Pt/ $C_{0.5}V_{2.24}CP$	11.53	57.23	1.48	0.73
$C_{0.5}V_{2.44}CP$	1.49	Pt/ $C_{0.5}V_{2.44}CP$	11.77	47.89	1.00	1.00
$C_{0.25}V_{2.24}CP$	8.16	Pt/ $C_{0.25}V_{2.24}CP$	8.19	75.87	1.94	1.94
$C_{1.0}V_{2.24}CP$	6.30	Pt/ $C_{1.0}V_{2.24}CP$	7.96	42.59	1.22	1.22
$C_{2.0}V_{2.24}CP$	5.21	Pt/ $C_{2.0}V_{2.24}CP$	9.25	28.07	0.45	0.45

In order to study the morphological changes on the surface of the CP substrate before and after activation, the CP substrates treated with different acidification voltages were analyzed by SEM. As shown in Figure 1e–h, during the rapid electrochemical acidification process, the carbon fiber structure gradually became rougher. As the voltage increased, deeper surface depressions and rougher surfaces were more conducive to the adsorption of Pt ions on the surface [24]. In this work, a higher acidification voltage was not used because it could no longer introduce more oxygen-containing functional groups, or the CP structure would become more brittle, making it no longer suitable as a substrate for Pt nanoparticles.

The changes in surface chemical composition of CP were studied by comparing the changes in the characteristic peaks during infrared testing before and after activation. According to Figure 2a,  $C_{0.5}V_{1.84}CP$ ,  $C_{0.5}V_{2.04}CP$ ,  $C_{0.5}V_{2.24}CP$  and  $C_{0.5}V_{2.44}CP$ , unlike  $C_{0.5}V_{0.24}CP$  and  $C_{0.25}V_{2.24}CP$ , all have a wide characteristic diffraction peak at  $1578\text{ cm}^{-1}$ , which represents the vibration mode of the C=O functional group, and a wide characteristic diffraction peak at  $2670\text{ cm}^{-1}$ , which represents the vibration mode of the -OH functional group [25]. These functional groups were introduced in the form of Equations (1)–(3) [26]. Such groups could form some chemical bonds on the surface of the carbon carrier, which helped to disperse and fixed metal ions on the carbon carrier. In order to make Pt particles more evenly dispersed and smaller, the acidification voltage and concentration were adjusted. It could be seen that low concentration acidification made it difficult to change the properties of carbon substrates. As shown in Figure 2b, compared to  $C_{0.5}V_{0.24}CP$ , the surface of  $C_{0.5}V_{2.24}CP$  not only has C=C/C-C bonds and C-OH, but also adds other oxygen-containing groups C=O and COOH. Among all oxygen-containing groups, the proportion of C=O groups was the highest, followed by C-OH and COOH. More active sites were extracted for the next deposition of Pt.

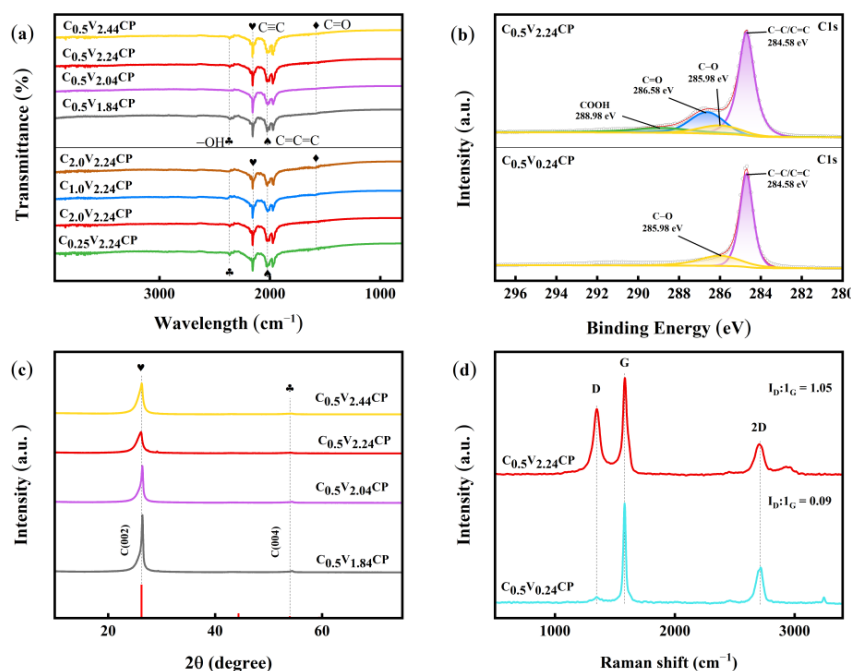
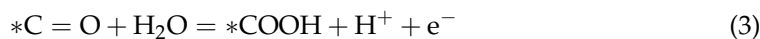
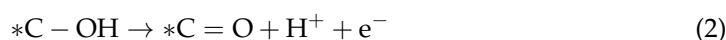
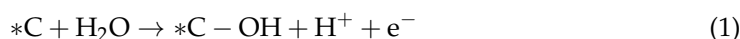


**Figure 2.** (a) Fourier transform infrared (FTIR) images of the activated CP substrates treated by different voltages and concentrations; (b) XPS C1s spectra  $C_{0.5}V_{0.24}CP$  and  $C_{0.5}V_{2.24}CP$ ; (c) X-ray diffraction detection (XRD) patterns of the  $C_{0.5}V_{1.84}CP$ ,  $C_{0.5}V_{2.04}CP$ ,  $C_{0.5}V_{2.24}CP$  and  $C_{0.5}V_{2.44}CP$ ; (d) Raman diagrams of the  $C_{0.5}V_{0.24}CP$  and  $C_{0.5}V_{2.24}CP$ .

As shown in Figure 2c, the peak value of CPs treated with different acidification conditions remains basically unchanged at the graphite C (002) crystal plane. Increasing the voltage cannot further expand the carbon layer spacing; however, as the electrochemical acidification voltage increased, the carbon peak height gradually decreased, indicating that acidification reduced the crystallinity of the graphite structure on the CP and increased the number of disordered carbon atoms on the surface of the CP [27].

To verify the increase in defects on CP after acidification, Raman characterization was performed on both no acidified and 2.24 V acidified CP. As shown in Figure 2d, compared with CP without acidification treatment ( $ID/IG = 0.09$ ),  $C_{0.5}V_{2.24}CP$  shows a higher integrated area ratio of D and G bands ( $ID/IG = 1.05$ ). With the  $sp^2$  degree of hybridization decreased, more defect sites in CP surface were formed [28]. Zheng et al. [29] demonstrated that carbon carrier surfaces with a large number of edge defect sites have certain oxygen reduction reaction (ORR) catalytic activity without any loaded metal. At the same time, defects on the surface of acidified CP can serve as the optimal sites for depositing metal ions, demonstrating the importance of edge carbon and structural defects in improving ORR activity.

## 2.2. Pt loaded on CP Substrates Treated under Different Acidification Concentrations and Voltages

In order to investigate whether oxygen-containing groups can provide better deposition sites for the deposition of Pt nanoparticles, an XPS investigation was conducted on catalysts deposited at different acidification voltages and different acidification concentrations. To investigate the C/O ratio affected by Pt loading, according to Figures S2 and S3 and Table 1, as the acidification voltage increases, the C/O ratio on the surface of CP first increases and then decreases. With the increase in sulfuric acid concentration or acidification voltage, the C/O ratio showed an increasing trend and the active sites provided for platinum loading were slightly reduced to avoid the aggregation of platinum particles aggravated by dense active sites. When the acidification voltage reached 2.44 V, the C/O ratio suddenly decreased, and the excessive acidification could lead to severe damage to the CP and a decrease in carbon content. During platinum deposition, oxygen-containing groups as active sites were occupied by Pt ions, resulting in a decrease in O1s after Pt is loaded on the CP substrate. In addition, during the deposition of Pt, oxygen-containing functional groups also continuously adsorbed/desorbed and competed with the process of Pt deposition [30]. Electrochemical acidification treatment of carbon substrates could reduce this unfavorable competition and improve deposition efficiency.

According to Figure 3a,b, the main binding energy peak centered on 284.6 eV corresponds to C–C/C=C, and the peak at a higher binding energy corresponds to carbon in the oxidation state. The peaks 286.2 eV and 290.1 eV correspond to C–OH and COOH, respectively [31,32]. After Pt deposition, the types of surface functional groups of catalysts without acidification treatment do not increase. After loading Pt, the C=O group was decreasing, indicating that C=O position was more likely to adsorb Pt ions and reduce Pt. In addition, the disappearance of C=O was also related to the high degree of oxidation on the surface of CP, leading to the partial generation of COOH [26].

To study the charge transfer between Pt and carbon fibers, XPS Pt4f spectroscopy analysis was performed on catalysts prepared. As shown in Figure 4a,b, judging the electron gain and loss of elements through peak displacement. The XPS spectra are characterized by a doublet containing a binding energy of Pt 4f7/2 (71.28–74.88 eV) and Pt 4f5/2 (74.58–78.38 eV), and the two peaks have a binding energy difference of 3.30 eV and a peak area ratio of 4:3 [33]. The results showed that the binding energy of the Pt 4f region decreased with the first increase in acidification voltage or acidification concentration. This change could increase the electron filling degree of the anti-bond energy band, thereby weakening the oxygen affinity of Pt, making the reaction intermediate easier to desorb and thus releasing the active site faster [34]. And when the acidification voltage or acidification concentration was too high, the binding energy would increase. It might be due to the high



degree of acidification causing too many defects on the CP and increasing the interaction force between Pt and CP [32].

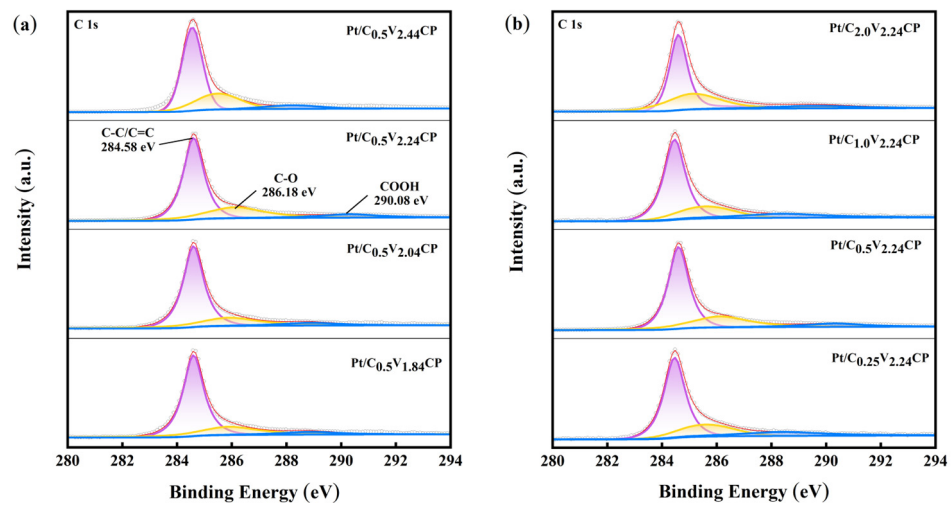


**Figure 3.** XPS C1s of (a) Pt/C<sub>0.5</sub>V<sub>1.84</sub>CP, Pt/C<sub>0.5</sub>V<sub>2.04</sub>CP, Pt/C<sub>0.5</sub>V<sub>2.24</sub>CP and Pt/C<sub>0.5</sub>V<sub>2.44</sub>CP and (b) Pt/C<sub>0.25</sub>V<sub>2.24</sub>CP, Pt/C<sub>0.5</sub>V<sub>2.24</sub>CP, Pt/C<sub>1.0</sub>V<sub>2.24</sub>CP and Pt/C<sub>2.0</sub>V<sub>2.24</sub>CP.

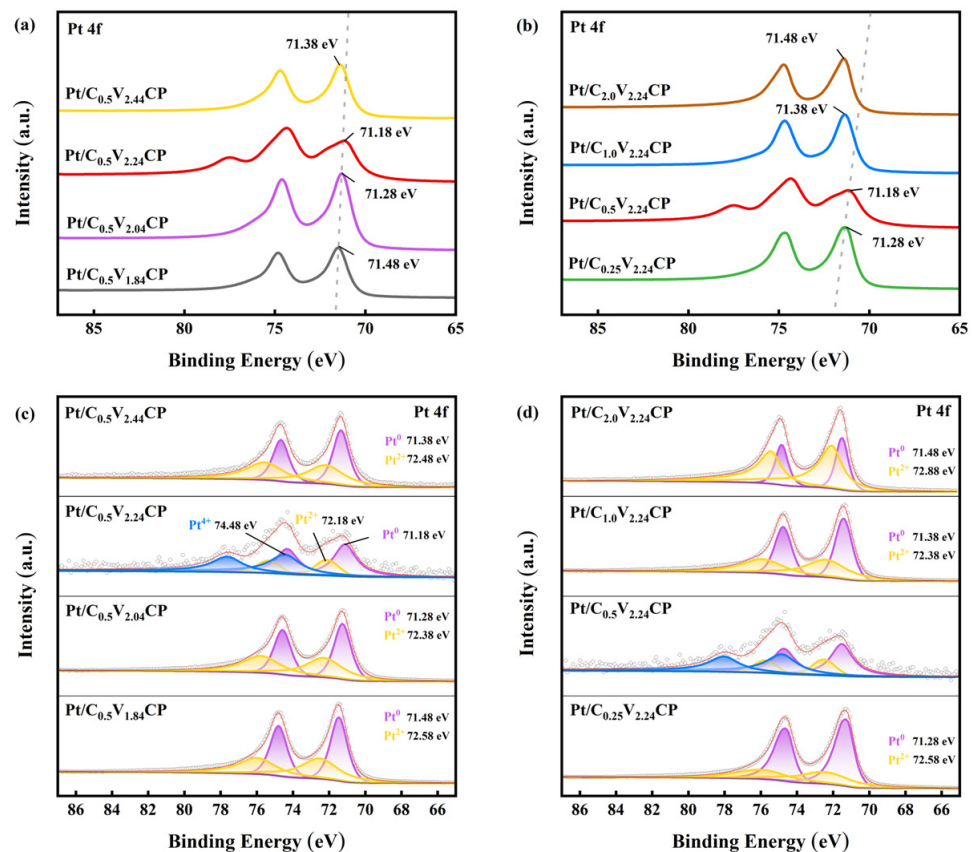


**Figure 4.** XPS (a) Pt4f and (c) deconvoluted Pt4f spectra of Pt/C<sub>0.5</sub>V<sub>1.84</sub>CP, Pt/C<sub>0.5</sub>V<sub>2.04</sub>CP, Pt/C<sub>0.5</sub>V<sub>2.24</sub>CP and Pt/C<sub>0.5</sub>V<sub>2.44</sub>CP; (b) Pt4f and (d) deconvoluted Pt4f spectra of Pt/C<sub>0.25</sub>V<sub>2.24</sub>CP, Pt/C<sub>0.5</sub>V<sub>2.24</sub>CP, Pt/C<sub>1.0</sub>V<sub>2.24</sub>CP and Pt/C<sub>2.0</sub>V<sub>2.24</sub>CP.

The Pt4f spectrum was deconvoluted into doublets labeled purple, yellow, and blue, which corresponded with Pt<sup>0</sup>, Pt<sup>2+</sup> (PtOH, PtO), and Pt<sup>4+</sup> (PtO<sub>2</sub>), respectively, as shown in Figure 4c,d. The ratios of Pt ions with different valence states are shown in Table 1.

The name of  $\text{Pt}^{2+}$  and  $\text{Pt}^{4+}$  were unified as  $\text{Pt}^{\delta+}$ . Because the chemical properties of Pt were stable, tetravalent Pt was unlikely to exist in the large amount  $\text{Pt}^0$ . The increase in acidification voltage caused the ratio of  $\text{Pt}^0$  to  $\text{Pt}^{2+}$  to first increase and then decrease, while the increase in acidification concentration caused the ratio of  $\text{Pt}^0$  to  $\text{Pt}^{2+}$  to first decrease and then increase. Since the adsorption of divalent platinum on oxygen molecules was closely related to the surface charge state of the catalyst, the balance between Pt adsorption of oxygen and the desorption of intermediate products OH and OOH could be controlled under the appropriate ratio of divalent Pt [35]. And in the frame of the chemical dissolution of PtO oxide proposed by Darling et al. [36], it was thus very likely that the surface PtO and  $\text{PtO}_2$  oxides act as a protecting layer for underlying Pt atoms at this potential and that the rate of Pt electro-oxidation was governed by chemical dissolution of PtO. Therefore, controlling the content of divalent platinum could appropriately exert the protective effect of  $\text{Pt}^{\delta+}$  on  $\text{Pt}^0$ , achieving good electrochemical performance.

In order to observe the surface morphology of platinum nanoparticles deposited after electrochemical acidification, SEM investigation was carried out. As shown in Figure 5a–d, Pt/ $\text{C}_{0.5}\text{V}_{0.24}\text{CP}$  platinum nanoparticles grow on rod-shaped carbon fibers exhibit a wide leaf-like structure with a larger particle size. Pt/ $\text{C}_{0.5}\text{V}_{1.84}\text{CP}$ , Pt/ $\text{C}_{0.5}\text{V}_{2.04}\text{CP}$  and Pt/ $\text{C}_{0.5}\text{V}_{2.24}\text{CP}$  exhibit uniform distribution of platinum nanoparticles on the surface of the carbon fibers and grow into nanoflower-like structures. As the acidification voltage increased, the nanoflowers became smaller and the platinum nanoparticles also became smaller. Platinum in Pt/ $\text{C}_{0.5}\text{V}_{2.44}\text{CP}$  could not be uniformly deposited on CP because the acidification voltage was too high, and during the acidification process, hydrogen bubbles would occupy the active sites that originally existed on the surface of the CP. The use of acidification voltage reduced the particle size of the deposited Pt, resulting in stronger nanoscale effects. As shown in Figure 5d–g, in the catalysts prepared at different acidification concentrations, Pt nanoparticles diameter decreases with the increase in acid concentration in the acidified CP. The PtNPs diameters of Pt/ $\text{C}_{0.25}\text{V}_{2.24}\text{CP}$ , Pt/ $\text{C}_{0.5}\text{V}_{2.24}\text{CP}$ , Pt/ $\text{C}_{1.0}\text{V}_{2.24}\text{CP}$ , and Pt/ $\text{C}_{2.0}\text{V}_{2.24}\text{CP}$  were 135.98, 56.63, 47.29, 45.46 nm, respectively. After the concentration reached 1 M, the particle size decreased while the platinum loading significantly decreased, which was unfavorable for ORR. As shown in Figure S4, all elements are uniformly distributed on the carbon fiber substrates.

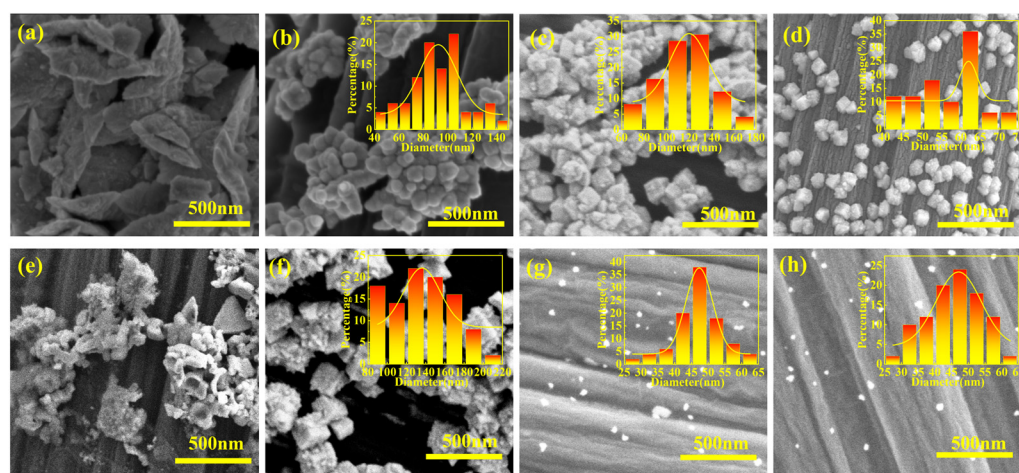


**Figure 5.** SEM images of (a) Pt/ $\text{C}_{0.5}\text{V}_{0.24}\text{CP}$ , (b) Pt/ $\text{C}_{0.5}\text{V}_{1.84}\text{CP}$ , (c) Pt/ $\text{C}_{0.5}\text{V}_{2.04}\text{CP}$ , (d) Pt/ $\text{C}_{0.5}\text{V}_{2.24}\text{CP}$ , (e) Pt/ $\text{C}_{0.5}\text{V}_{2.44}\text{CP}$ , (f) Pt/ $\text{C}_{0.25}\text{V}_{2.24}\text{CP}$ , (g) Pt/ $\text{C}_{1.0}\text{V}_{2.24}\text{CP}$  and (h) Pt/ $\text{C}_{2.0}\text{V}_{2.24}\text{CP}$ .

The crystal structures of the catalysts were tested using XRD investigation. As shown in Figure 6a, it is confirmed through jade analysis that face-centered cubic Pt has been synthesized for different catalyst electrodes. The strongest absorption characteristic peak of the Pt (111) crystal plane indicated that Pt mainly grows along the (111) crystal plane. With the acidification voltage increased, the intensities of the Pt (111), Pt (200), and Pt (220)

peaks decreased, which indicate that the decrease in crystal particle size improved the utilization efficiency of surface platinum. With the increase in sulfuric acid concentration during the acidification process, the peak intensity of platinum first decreased and then increased. Combined with SEM (Figure 5f,g), it can be seen that a low acid concentration leads to high platinum crystallization and agglomeration. Although platinum particles prepared with high acid concentration have a high crystallization degree, the loading is too low. Overall, it is not conducive to the improvement of ORR activity. When the sulfuric acid concentration during the acidification process is 0.5 M, its 2θ maximum results in a stronger interaction between the carbon matrix and Pt [37,38]. In addition, it is evident that as the acidification voltage increases, the platinum peak shifts towards a positive direction, indicating an enhanced stretching effect between platinum and carbon carriers. This can be ascribed to the appearance of chemical-induced tensile strain into Pt lattice [39].

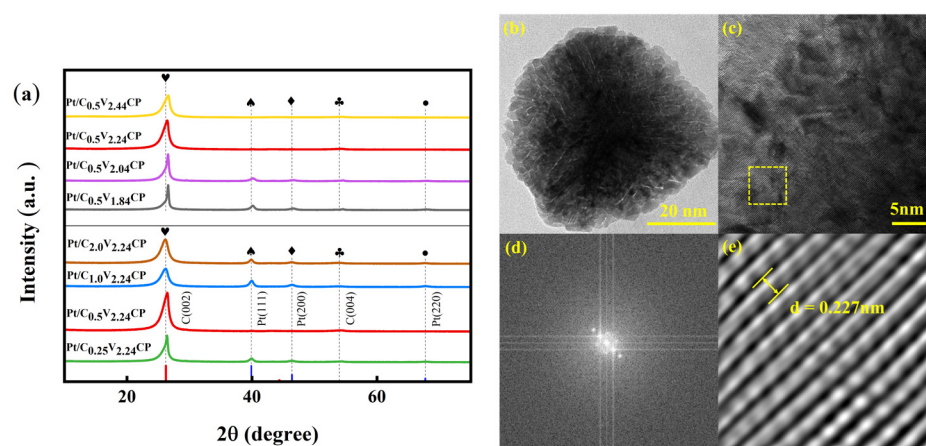


**Figure 6.** (a) XRD patterns of the Pt/C<sub>0.5</sub>V<sub>1.84</sub>CP, Pt/C<sub>0.5</sub>V<sub>2.04</sub>CP, Pt/C<sub>0.5</sub>V<sub>2.24</sub>CP, Pt/C<sub>0.5</sub>V<sub>2.44</sub>CP, Pt/C<sub>0.25</sub>V<sub>2.24</sub>CP, Pt/C<sub>1.0</sub>V<sub>2.24</sub>CP and Pt/C<sub>2.0</sub>V<sub>2.24</sub>CP; (b) 20 nm scale and (c) 5 nm scale images of the transmission electron microscopy (TEM) of Pt/C<sub>0.5</sub>V<sub>2.04</sub>CP; (d) the two-dimensional vector projection in the frequency space for the selected area in (c); (e) the corresponding inverse fast Fourier transformation (FFT) diagram of this area.

To further demonstrate the preferential growth of the Pt (111) surface of Pt nanoparticles, the Pt/C<sub>0.5</sub>V<sub>2.24</sub>CP catalyst with the best electrochemical activity was selected for TEM investigation. As shown in Figure 6b, it can be clearly observed that the particle size of nano Pt is ~60 nm, which is close to the average particle size of 56.63 nm in SEM statistics, and it has the morphological characteristics of a regular tetrahedron. During the fast Fourier transformation (FFT) process, we obtain the two-dimensional projection vectors (Figure 6d) in the frequency space of TEM images and the corresponding inverse FFT diagram (Figure 6e). Figure 5e shows the crystal plane spacing was measured to be 0.227 nm, corresponding to the Pt (111) crystal plane, which is consistent with the XRD analysis results.

### 2.3. Half-Cell Electrochemical Tests of Catalyst Electrodes

Figure 7a shows the typical CV responses recorded between 0.03 and 1.2 V for the CP substrates prepared under different acidification voltages. C<sub>0.5</sub>V<sub>0.24</sub>CP, C<sub>0.5</sub>V<sub>1.84</sub>CP, C<sub>0.5</sub>V<sub>2.04</sub>CP, and C<sub>0.5</sub>V<sub>2.24</sub>CP all exhibited a pair of clear oxidation and reduction peaks at ~0.6 V, which could be attributed to the presence of carbon–oxygen functional groups on the surface of the CP. Moreover, as the acidification voltage increased, the current density gradually increased, which was the result of the joint action of small defects, oxygen-containing functional groups, and other factors on the CP. At the same time, the area of the double electric layer and hydrogen region of the CP substrate increased with the increase in the acidification voltage because electrochemical acidification improved the properties of the carbon material by making its capacitance larger and increasing its active sites. When



the acidification voltage was increased to 2.44 V, the redox peak area was close to that at 2.24 V, which indicated that further increasing the acidification voltage was of little use for improving electrochemical performance. And according to Figure S6, the increase in acidification concentration directly leads to significant changes in the double layer range and hydrogen region area of the CP substrate, thereby increasing the electrochemical active area of the CP substrate.

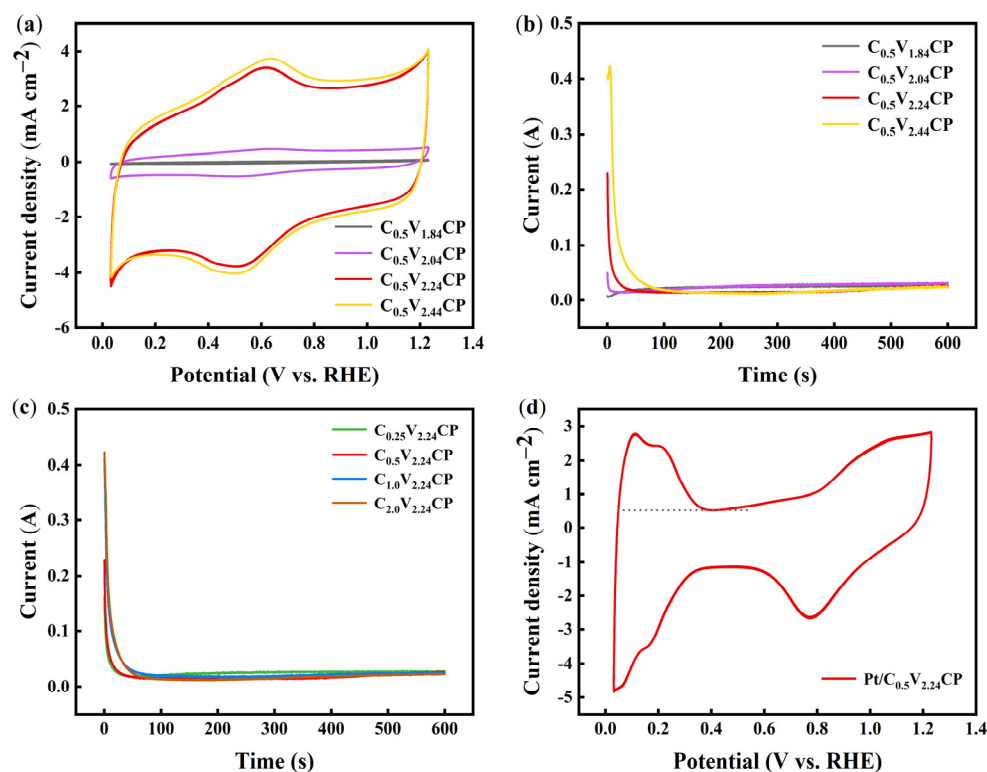


**Figure 7.** (a) Cyclic voltammetry (CV) diagrams of C<sub>0.5</sub>V<sub>1.84</sub>CP, C<sub>0.5</sub>V<sub>2.04</sub>CP, C<sub>0.5</sub>V<sub>2.24</sub>CP and C<sub>0.5</sub>V<sub>2.44</sub>CP in 0.5 M H<sub>2</sub>SO<sub>4</sub>, 100 mV·s<sup>-1</sup> scan speed and Ar environment; (b) Process curves of Pt deposition on C<sub>0.5</sub>V<sub>1.84</sub>CP, C<sub>0.5</sub>V<sub>2.04</sub>CP, C<sub>0.5</sub>V<sub>2.24</sub>CP and C<sub>0.5</sub>V<sub>2.44</sub>CP; (c) Process curves of Pt deposition on C<sub>0.25</sub>V<sub>2.24</sub>CP, C<sub>0.5</sub>V<sub>2.24</sub>CP, C<sub>1.0</sub>V<sub>2.24</sub>CP and C<sub>2.0</sub>V<sub>2.24</sub>CP; (d) CV diagrams of Pt/C<sub>0.5</sub>V<sub>2.24</sub>CP in 0.5 M H<sub>2</sub>SO<sub>4</sub>, 100 mV·s<sup>-1</sup> scan speed and Ar environment.

As shown in the process curve of Pt deposition in Figure 7b,c, in the early stage of the deposition process, the maximum current represents nucleation on newly deposited Pt crystals. Later, the current decreases to the lowest and then increases upwards and gradually stabilizes, indicating that secondary crystal nucleation and growth of Pt begin to occur on CP, mainly under diffusion control. The maximum deposition currents of Pt/C<sub>0.5</sub>V<sub>0.24</sub>CP, Pt/C<sub>0.5</sub>V<sub>1.84</sub>CP, Pt/C<sub>0.5</sub>V<sub>2.04</sub>CP, and Pt/C<sub>0.5</sub>V<sub>2.24</sub>CP are 0.00 A, 0.01 A, 0.05 A, 0.23, and 0.42 A (Table 2), respectively. As the acidification potential increased, the maximum current peak became larger. Among them, the CP treated with 2.24 V voltage acidification better nucleated the deposited Pt. The initial deposition currents of Pt/C<sub>0.25</sub>V<sub>2.24</sub>CP, Pt/C<sub>0.5</sub>V<sub>2.24</sub>CP, Pt/C<sub>1.0</sub>V<sub>2.24</sub>CP, and Pt/C<sub>2.0</sub>V<sub>2.24</sub>CP are 0.16 A, 0.23 A, 0.41 A, and 0.42 A (Table 2), respectively. As the acidification concentration increased, the initial current grew larger, and it became easier to grow smaller Pt nuclei. However, its nucleation time also increased. If this process had continued for too long, it would cause further growth of Pt nuclei, reducing the nanoscale effect of the oxygen reduction catalyst in this experiment [40]. The CP substrates exhibited a rather low electric conductivity, leading to a relatively high double-layer capacitance observed in CV. Nevertheless, the hydrogen adsorption used for the determination of ECSA was well defined, as shown in Figure 7d.

**Table 2.** Summary of initial deposition current in deposition process,  $Pt_{loading}$ , electrochemical active surface area (ECSA), onset potential, and Tafel slope of different catalysts before and after accelerated durability testing (ADT).

Catalyst	Initial Deposition Current A	Before ADT				After ADT		
		$Pt_{loading}$ mg/cm <sup>2</sup>	ECSA m <sup>2</sup> /g <sub>Pt</sub>	$E_{onset}$ V vs. RHE	Tafel Slop mV dec <sup>−1</sup>	ECSA m <sup>2</sup> /g <sub>Pt</sub>	$E_{onset}$ V vs. RHE	Tafel Slop mV dec <sup>−1</sup>
Pt/C <sub>0.5</sub> V <sub>0.24</sub> CP	0.00	0.24	11.86	0.89	63.51	7.39	0.87	58.20
Pt/C <sub>0.5</sub> V <sub>1.84</sub> CP	0.01	0.20	12.40	0.84	84.02	7.33	0.80	74.27
Pt/C <sub>0.5</sub> V <sub>2.04</sub> CP	0.05	0.13	12.60	0.86	82.58	12.35	0.83	76.27
Pt/C <sub>0.5</sub> V <sub>2.24</sub> CP	0.23	0.06	49.35	0.91	74.26	36.11	0.87	81.47
Pt/C <sub>0.5</sub> V <sub>2.44</sub> CP	0.42	0.05	124.46	0.86	94.56	85.80	0.80	122.46
Pt/C <sub>0.25</sub> V <sub>2.24</sub> CP	0.16	0.14	25.72	0.90	71.94	11.45	0.87	81.86
Pt/C <sub>1.0</sub> V <sub>2.24</sub> CP	0.41	0.03	241.72	0.91	78.66	116.63	0.77	87.34
Pt/C <sub>2.0</sub> V <sub>2.24</sub> CP	0.42	0.02	270.99	0.88	102.11	171.24	0.75	124.51
Pt/C/CP-1	-	0.10	12.40	0.87	96.56	5.86	0.85	110.20
Pt/C/CP-2	-	0.10	16.92	0.85	93.80	5.97	0.84	82.26

The ECSA of different catalyst electrodes of Pt (Table 2) is comparable with what is found in literature [41], showing that despite the electrodeposited catalysts having a large particle size, the Pt utilization is high. And compared with commercial Pt/C coated in CP (Figure S5), Pt/C<sub>0.5</sub>V<sub>2.24</sub>CP and Pt/C<sub>0.25</sub>V<sub>2.24</sub>CP had a larger ECSA, which showed better activity. The Pt/C<sub>0.5</sub>V<sub>2.24</sub>CP exhibits the highest onset potential and the lowest Tafel slope, as shown in Figure 8b. Furthermore, the advantage of electrodeposited Pt/C<sub>0.5</sub>V<sub>2.24</sub>CP NPs becomes apparent when the Pt mass activity at ORR is considered (Figure 8a). This is because sufficient electrochemical acidification made the surface of CP rich in more uniform oxygen-containing groups. These functional groups could promote the preferential adsorption of Pt ions to these positions for uniform nucleation, while oxygen-containing functional groups also played a certain limiting role in the growth of platinum particles, which made the size of Pt nanoparticles loaded by electrodeposition smaller [37], which was beneficial for improving the electrochemical performance of oxygen reduction catalysts.

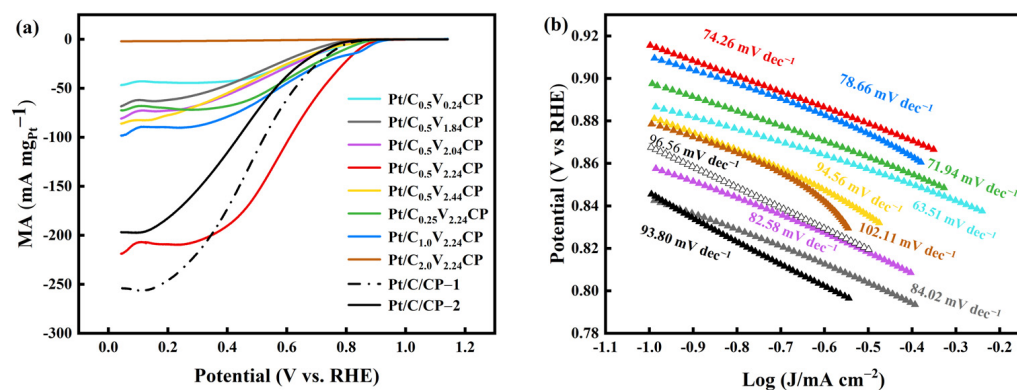


**Figure 8.** (a) The mass activity and (b) Tafel slope of different catalyst electrodes, commercial Pt/C/CP-1 and Pt/C/CP-2 before 5000 cycles aging in 0.5 M H<sub>2</sub>SO<sub>4</sub>, 10 mV·s<sup>−1</sup> sweep rate, O<sub>2</sub> environment.

The durability of the oxygen reduction catalysts determines the practical application value of fuel cells. According to Figure 9a, it can be seen that the ECSA of all the catalyst electrodes decreases after 5000 cycles ADT. Considering the initial value and attenuation degree of ECSA, Pt/C<sub>0.5</sub>V<sub>2.24</sub>CP had a high ECSA value at first and maintained it at 36.11 m<sup>2</sup>/g<sub>Pt</sub>, which was a good ECSA after 5000 cycles ADT for a catalyst electrode. According to Table 2, Pt/C<sub>0.5</sub>V<sub>2.24</sub>CP and Pt/C<sub>0.25</sub>V<sub>2.24</sub>CP have the highest onset potential and still maintain good performance after ADT. The catalysts Pt/C<sub>0.5</sub>V<sub>0.24</sub>CP, Pt/C<sub>0.5</sub>V<sub>1.84</sub>CP,



neutral with deionized water and dried in an oven. Figure 10 shows the schematic diagram for the synthesis processes.

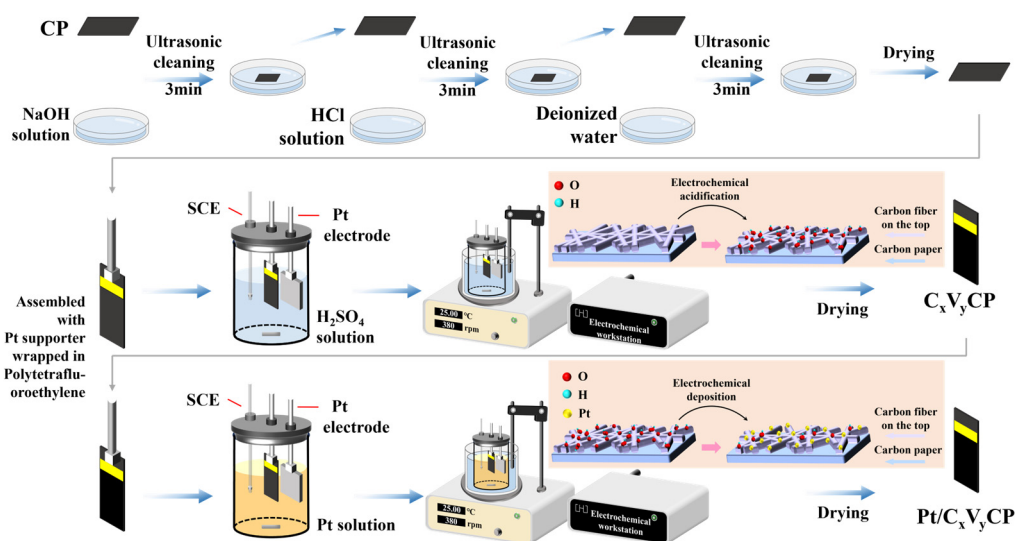


**Figure 10.** Schematic diagram for the synthesis processes and synthesis route (red background).

The acidification and electrodeposition of CPs were performed by constant voltage treatment from aqueous solution in a three-electrode electrochemical cell. An electrochemical workstation CHI660e was used with a  $2 \times 2 \text{ cm}^2$  platinum sheet as the counter electrode (CE), a saturated calomel electrode (SCE) as the reference electrode (RE), and a working electrode (WE). The WE consisted of the cleaned CP, mounted on a platinum electrode clamp, which was the platinum supporter wrapped in polytetrafluoroethylene, to ensure electrical connection, and a homogeneous charge distribution over the entire area of the CP during acidification. The area submerged in the electrolyte of the CP was  $1 \times 2 \text{ cm}^2$  and the excessive area was isolated with polyimide tape (Figure S8 in the Supporting Information).

Electrochemical acidification was carried out in a 120 mL three-electrode electrolytic cell containing 0.25–2 M  $\text{H}_2\text{SO}_4$  solution, with a rotational speed of 380 rpm. And the voltage was set to 1.84–2.44 V (vs. RHE, all potentials in the text, figures, and tables were converted to vs. RHE.) for 300 s. The temperature was kept constant at  $25^\circ\text{C}$  by using a thermostat. The CP processed in this way were named  $\text{C}_x\text{V}_y\text{CP}$  (x: the concentration of sulfuric acid solution, M; y: the acidification voltage, V vs. RHE).

For the electrodeposition of platinum, the aqueous electrolytes were loaded with 0.1 M KCL, 0.5 M  $\text{H}_2\text{SO}_4$ , 2 mM  $\text{H}_2\text{PtCl}_6 \cdot 6\text{H}_2\text{O}$ , and 60 mM DMF. Nano Pt particles were electrodeposited on the  $\text{C}_x\text{V}_y\text{CP}$  substrates using a constant voltage method, with a working voltage set to  $-0.04 \text{ V}$  for 600 s and maintained at a speed of 380 rpm. After electrodeposition was complete, the CP was taken out and soaked in deionized water for 30 min to remove impurities on the surface. The temperature was kept constant at  $25^\circ\text{C}$  using a thermostat. The CP was then dried at  $80^\circ\text{C}$  for 12 h in an oven to obtain a catalyst electrode named  $\text{Pt}/\text{C}_x\text{V}_y\text{CP}$ .

### 3.3. Preparation of Commercial Catalyst Electrodes

CPs are also used as a carrier for commercial platinum carbon catalyst coating. The specific preparation process is as follows:

Take 5 mg of the commercial catalyst Pt/C into a centrifuge tube and add 500  $\mu\text{L}$  of deionized water and 500  $\mu\text{L}$  isopropanol. Then, sonicate for 1 h to obtain a commercial catalyst slurry. Apply 100  $\mu\text{L}$  of the commercial catalyst slurry onto the cleaned CP substrate ( $1 \times 1 \text{ cm}^2$ ) on both sides. Dry the CP which is applied to the commercial catalyst at  $80^\circ\text{C}$  for 12 h in an oven, and then fix it on a platinum electrode clamp to obtain a commercial catalyst electrode without the Nafion solution.



This commercial catalyst electrode would be named Pt/C/CP-1, with a loading capacity of about  $0.1 \text{ mg}_{\text{Pt}} \cdot \text{cm}^{-1}$ . Usually, commercial catalysts need to be loaded onto CP using polymer solutions such as Nafion to avoid the detachment of commercial catalysts during the actual reaction process.

For comparison, the 25  $\mu\text{L}$  Nafion solution is added to the above-mentioned commercial catalyst slurry solution to prepare a commercial catalyst electrode, named Pt/C/CP-2, with a loading capacity about  $0.1 \text{ mg}_{\text{Pt}} \cdot \text{cm}^{-1}$ .

### 3.4. Electrochemical Test

The three-electrode set-up used for the electrochemical test consisted of a platinum wire electrode, which was CE, a SCE as RE, and a WE. The WE was the catalyst electrode clamped by the platinum electrode clamp and kept immersed in the electrolyte area of  $1 \times 0.5 \text{ cm}^2$ .

The CV was used to activate the catalyst electrodes and to determine their ECSA by Equation (4) in a 0.5 M  $\text{H}_2\text{SO}_4$ . To this end, 20 cycles at 100 mV/s and 6 cycles at 100 mV/s were recorded in a potential window between 0.03 and 1.2 V versus the reversible hydrogen electrode (RHE). ORR was studied by CV in  $\text{O}_2$ -saturated 0.5 M  $\text{H}_2\text{SO}_4$  after recording a background CV in Ar-saturated electrolyte, both at 100 mV/s between 0 and 1.1 V and in static conditions. The prepared catalyst electrodes were placed in a 0.5 M  $\text{H}_2\text{SO}_4$  solution saturated with oxygen, and ADT was conducted using CV. The operating conditions were 0.6–1.0 V in an acidic environment of 0.5 M  $\text{H}_2\text{SO}_4$ , with a scanning rate of  $100 \text{ mV} \cdot \text{s}^{-1}$  for 5000 cycles. The potential corresponding to a current density of  $-0.1 \text{ mA} \cdot \text{cm}^{-2}$  is taken as the onset potential. The Tafel curve is transformed from the LSV curve.

$$\text{ECSA} = \frac{S_{\text{H}}}{C \cdot V \cdot m_{\text{Pt}}} \quad (4)$$

$S_{\text{H}}$ : area of hydrogen desorption peak,  $\text{A} \cdot \text{V}$ ;  $V$ : scanning speed,  $\text{V} \cdot \text{s}^{-1}$ ;  $C$ :  $0.21 \text{ mC} \cdot \text{cm}^{-2}$ ;  $m_{\text{Pt}}$ : the loading of Pt on the working electrode, g.

It should be noted that the procedure for ORR measurements employed here differs from the usual approach using rotating disk electrode (RDE) since the electrocatalysts are directly deposited onto the gas diffusion layer substrates and cannot be deposited directly onto an RDE. As a result, a quantitative determination of the ORR parameters, such as the half-wave potential, is not feasible. Nevertheless, the measurements give qualitative information to show trends between catalysts of different compositions, in addition to the comparison with a commercial catalyst electrode.

### 3.5. Characterizations and Measurements

Pt loading on the self-made catalysts was determined by the inductively coupled plasma mass spectrometry (ICP-MS, Perkinelmer Co., Ltd., Waltham MA, USA) with Equation (5). The catalyst microstructure and the size of Pt nanoparticles were detected using a TEM (JEM-F200, Jeol Ltd., Tokyo, Japan), and the catalyst morphology was observed on a field emission field emission SEM (Nova NanoSEM 450, FEI, Hillsboro, OR, USA). The energy-dispersive X-ray Spectroscopy (EDS, ZEISS Sigma 300, Zeiss Ltd., Oberkochen, Germany) was used to characterize the elemental composition of the samples. The XRD method was applied to characterize the carbon phase and crystal phase, which was fulfilled by adopting copper target radiation ( $\lambda = 0.15405 \text{ nm}$ ) along with an operative voltage of 40 kV and a current of 40 mA. The scanning range was  $2\theta = 10\text{--}80^\circ$  and the scanning rate was  $\omega = 5^\circ \text{min}^{-1}$ . FTIR (Nicolet iS10, Thermo Fisher Scientific, Waltham, MA, USA) spectra were taken to analyze and characterize the chemical composition of CP in the attenuated total reflection (ATR) mode over a spectral range with a wave number of 4000 to  $400 \text{ cm}^{-1}$ . XPS (Thermo Scientific K-Alpha, Thermo Fisher Scientific, Waltham, MA, USA) was used to analyze the surface chemical elements of catalysts. And sample charging was corrected using the C1s peak at 284.8 eV as reference. Raman spectroscopy was conducted with

Horiba LabRAM HR Evolution (Horiba, Kyoto, Japan) laser Raman spectrometer by using a 633 nm He-Ne laser with wave number range of 500 to 3500  $\text{cm}^{-1}$ .

$$m_{\text{loading}} = \frac{C_0 \cdot V_0}{S_{\text{sample}}} \quad (5)$$

$m_{\text{loading}}$ : Pt loading on catalyst electrodes,  $\text{mg} \cdot \text{cm}^{-2}$ ;  $C_0$ : concentration of Pt in the test solution was obtained by ICP-MS testing,  $\text{mg} \cdot \text{L}^{-1}$ ;  $V_0$ : volume of digestion solution at constant volume, mL;  $S_{\text{sample}}$ : area of catalyst electrode sample,  $\text{cm}^2$ .

#### 4. Conclusions

This work provided a novel method for preparing oxygen reduction catalysts through electrochemical acidification synergistic electrodeposition (Figure 10). By selecting a CP substrate with a self-supporting structure as the catalyst carrier, an electrochemical acidification technique was used to first oxidize the surface of the CP, making it rich in oxygen-containing groups, such as hydroxyl, carbonyl, and carboxyl groups, providing more active sites and introducing heteroatoms for the next step of depositing platinum particles. Due to the special properties of the CP treated with electrochemical acidification in the previous step, the polarization curve of the Pt electrodeposition in the next step showed a high current in the early stage of deposition, which enabled more Pt nanoparticles to form very small nanoparticle nuclei on the surface of the CP, promoting the uniform distribution of Pt on the carrier and the nanoscale uniformity.

During the deposition of Pt, as the acidification potential increased, the maximum current peak became larger, resulting in a better nucleation effect for Pt. In LSV testing, Pt/ $\text{C}_{0.5}\text{V}_{2.24}\text{CP}$  showed a higher initial potential due to sufficient electrochemical acidification, which enriched the surface of the CP with more uniform oxygen-containing groups and activated the chemically inert carbon surface. The Tafel slope for Pt/ $\text{C}_{0.5}\text{V}_{2.24}\text{CP}$  was  $74.26 \text{ mV} \cdot \text{dec}^{-1}$ , which shows that the catalyst electrode has good kinetic efficiency. The initial starting potentials of Pt/ $\text{C}_{0.5}\text{V}_{2.24}\text{CP}$  were 40 mV and 50 mV higher than those of Pt/C/CP-1 and Pt/C/CP-2, respectively. The mass activities were 1.74 times and 1.78 times higher than those of Pt/C/CP-1 and Pt/C/CP-2, respectively. The starting potentials after aging were 20 mV and 30 mV higher, respectively. This proves that Pt grown by electrodeposition on CP can anchor more firmly on the CP. In summary, the acidification of CP under the appropriate conditions of 0.5 M  $\text{H}_2\text{SO}_4$  acid and 2.24 can obtain the preferred substrate for electrodeposition of platinum, so that the combined catalyst electrode has good ORR activity.

Compared with the traditional method, this novel method not only reduced the manufacturing cost by taking the preparation of catalyst and the combination of catalyst with GDL as one step, but also greatly shortened the preparation time. The preparation time of the catalyst electrode was 15 min, which is far less than the hours required for the preparation of traditional electrodes, and this provides a promising prospect for the more convenient and effective preparation of the cathode catalyst electrodes.

#### 5. Patents

The results of this research are part of the patent applications “A method for preparing oxygen reduction catalysts through electrochemical acidification and synergistic electrodeposition” related to CN115939429B.

**Supplementary Materials:** The following supporting information can be downloaded at: <https://www.mdpi.com/article/10.3390/catal14050300/s1>, Figure S1: XPS full spectra of (a)  $\text{C}_{0.5}\text{V}_{0.24}\text{CP}$  and (b)  $\text{C}_{0.5}\text{V}_{2.24}\text{CP}$ ; Figure S2: XPS full spectra of (a) Pt/ $\text{C}_{0.5}\text{V}_{0.24}\text{CP}$ , (b) Pt/ $\text{C}_{0.5}\text{V}_{1.84}\text{CP}$ , (c) Pt/ $\text{C}_{0.5}\text{V}_{2.04}\text{CP}$  and (d) Pt/ $\text{C}_{0.5}\text{V}_{2.24}\text{CP}$  catalysts; Figure S3: XPS full spectra of (a) Pt/ $\text{C}_{0.25}\text{V}_{2.24}\text{CP}$ , (b) Pt/ $\text{C}_{0.5}\text{V}_{2.24}\text{CP}$ , (c) Pt/ $\text{C}_{1.0}\text{V}_{2.24}\text{CP}$  and (d) Pt/ $\text{C}_{2.0}\text{V}_{2.24}\text{CP}$  catalysts; Figure S4: Mapping diagram of Pt/ $\text{C}_{2.0}\text{V}_{2.24}\text{CP}$  catalyst electrode; Figure S5: CV diagram of  $\text{C}_{0.25}\text{V}_{2.24}\text{CP}$ ,  $\text{C}_{0.5}\text{V}_{2.24}\text{CP}$ ,  $\text{C}_{1.0}\text{V}_{2.24}\text{CP}$  and  $\text{C}_{2.0}\text{V}_{2.24}\text{CP}$  in 0.5 M  $\text{H}_2\text{SO}_4$ ,  $100 \text{ mV} \cdot \text{s}^{-1}$  sweep rate in Ar environment; Figure S6: CV diagram of commercial

catalysts in 0.5 M H<sub>2</sub>SO<sub>4</sub>, 100 mV·s<sup>−1</sup> sweep rate in Ar environment; Figure S7: SEM images of the (a) Pt/C<sub>0.5</sub>V<sub>0.24</sub>CP, (b) Pt/C<sub>0.5</sub>V<sub>1.84</sub>CP, (c,d) different areas of Pt/C<sub>0.5</sub>V<sub>2.04</sub>CP after ADT; Figure S8: Set-up of the three-electrode electrochemical cell with the Pt counter electrode (CE), SCE reference electrode (RE) and CP working electrode (WE).

**Author Contributions:** Writing—Original Draft, L.Z.; Conceptualization, L.Z.; Methodology, L.Z., Y.G. and Y.X.; Validation, L.Z. and Y.G.; Investigation, L.Z., Y.G. and Y.X.; Writing—Review and Editing, P.L. and Q.Z.; Project Administration, P.L. and Q.Z.; Supervision, P.L. and Q.Z. All authors have read and agreed to the published version of the manuscript.

**Funding:** This research received no external funding.

**Data Availability Statement:** The raw data supporting the conclusions of this article will be made available by the authors on request.

**Acknowledgments:** The authors extend their gratitude to the National Key R&D Program of China (2023YFB4006101).

**Conflicts of Interest:** The authors declare no competing financial conflicts of interest.

## References

1. Guan, D.Q.; Wang, B.W.; Zhang, J.G. Hydrogen society: From present to future. *Energy Environ. Sci.* **2023**, *16*, 4926–4943. [\[CrossRef\]](#)
2. Junbo, H.; Min, Y.; Changchun, K.; Guanghua, W.; Cameron, P.; Zhi, Q.; Gang, W.; Junliang, Z. Platinum-group-metal catalysts for proton exchange membrane fuel cells: From catalyst design to electrode structure optimization. *Energychem* **2020**, *2*, 10023–10061.
3. Yaldagard, M.; Seghatoleslami, N.; Jahanshahi, M. Oxygen Reduction Reaction Activity Improvement in Cu/PtPd Nanocatalyst Based on Core-Shell Structured through Electrochemical Synthesis on Porous Gas Diffusion Electrodes in Polymer Electrolyte Membrane Fuel Cells. *J. Nano Res.* **2015**, *31*, 61–80. [\[CrossRef\]](#)
4. Rego, R.; Oliveira, C.; Velázquez, A.; Cabot, P. A new route to prepare carbon paper-supported Pd catalyst for oxygen reduction reaction. *Electrochim. Commun.* **2010**, *12*, 745–748. [\[CrossRef\]](#)
5. Ferrero, G.A.; Diez, N.; Sevilla, M.; Fuertes, A.B. Iron/Nitrogen co-doped mesoporous carbon synthesized by an endo-templating approach as an efficient electrocatalyst for the oxygen reduction reaction. *Microporous Mesoporous Mater.* **2019**, *278*, 280–288. [\[CrossRef\]](#)
6. Podleschny, P.; Rost, U.; Muntean, R.; Marginean, G.; Heinze, A.; Peinecke, A.; Radev, I.; Muhler, M.; Brodmann, M. Investigation of Carbon Nanofiber-supported Electrocatalysts with Ultra-low Platinum Loading for the Use in PEM Fuel Cells. *Fuel Cell* **2018**, *5*, 586–593. [\[CrossRef\]](#)
7. Lüsi, M.; Erikson, H.; Merisalu, M.; Rahn, M.; Sammelselg, V.; Tammeveski, K. Electrochemical reduction of oxygen in alkaline solution on Pd/C catalysts prepared by electrodeposition on various carbon nanomaterials. *J. Electroanal. Chem.* **2019**, *834*, 223–232. [\[CrossRef\]](#)
8. Kim, Y.; Lee, H.; Lim, T.; Kim, H.; Kwon, O.J. Non-conventional Pt-Cu alloy/carbon paper electrochemical catalyst formed by electrodeposition using hydrogen bubble as template. *J. Power Sources* **2017**, *364*, 16–22. [\[CrossRef\]](#)
9. YohRong, L.; YangChih, H.; TsongPyng, P. Fabrication of TiN inverse opal structure and Pt nanoparticles by atomic layer deposition for proton exchange membrane fuel cell. *Int. J. Hydrogen Energy* **2017**, *42*, 10175–10183.
10. Suvani, S.; Rashika, S.; Dipak, K.G.; Amit, K.D.; Narayan, C.D. Electrodeposited Cu<sub>2</sub>O Nanopetal Architecture as a Superhydrophobic and Antibacterial Surface. *Langmuir* **2019**, *35*, 17166–17176.
11. Ganesan, A.; Narayanasamy, M.; Shunmugavel, K. Self-humidifying manganese oxide-supported Pt electrocatalysts for highly-durable PEM fuel cells. *Electrochim. Acta* **2018**, *285*, 47–59. [\[CrossRef\]](#)
12. Muthukumar, V.; Chetty, R. Morphological transformation of electrodeposited Pt and its electrocatalytic activity towards direct formic acid fuel cells. *J. Appl. Electrochem.* **2017**, *47*, 735–745. [\[CrossRef\]](#)
13. Weiser, M.; Schulze, C.; Schneider, M.; Michaelis, A. Platinum electrodeposition from a dinitrosulfatoplatinate(II) electrolyte. *Appl. Surf. Sci.* **2016**, *390*, 333–338. [\[CrossRef\]](#)
14. Liu, J.; Wang, X.; Lin, Z.; Cao, Y.; Zheng, Z.; Zeng, Z.; Hu, Z. Shape-Controllable Pulse Electrodeposition of Ultrafine Platinum Nanodendrites for Methanol Catalytic Combustion and the Investigation of their Local Electric Field Intensification by Electrostatic Force Microscope and Finite Element Method. *Electrochim. Acta* **2014**, *136*, 66–74. [\[CrossRef\]](#)
15. Sookhakian, M.; Ridwan, N.A.; Zalnezhad, E.; Yoon, G.H.; Azarang, M.; Mahmoudian, M.R.; Alias, Y. Layer-by-Layer Electrodeposited Reduced Graphene Oxide-Copper Nanopolyhedra Films as Efficient Platinum-Free Counter Electrodes in High Efficiency Dye-Sensitized Solar Cells. *J. Electrochem. Soc.* **2016**, *163*, D154–D159. [\[CrossRef\]](#)

16. Su, Y.; Ren, H.; Jiang, H.; Tang, S.; Lu, H.; Meng, X. Two-Stage Tunneling-Dominated Electrodeposition for Large-Scale Production of Ultralong Wavy Metal Microstructures on Native Oxide Layer-Passivated Si Electrode with Specific Surface Configuration. *J. Phys. Chem. C* **2019**, *123*, 16326–16331. [\[CrossRef\]](#)
17. Hay, C.E.; Lee, J.; Silvester, D.S. Formation of 3-Dimensional Gold, Copper and Palladium Microelectrode Arrays for Enhanced Electrochemical Sensing Applications. *Nanomaterials* **2019**, *9*, 1170. [\[CrossRef\]](#) [\[PubMed\]](#)
18. Michalak, M.; Roguska, A.; Nogala, W.; Opallo, M. Patterning Cu nanostructures tailored for CO<sub>2</sub> reduction to electrooxidizable fuels and oxygen reduction in alkaline media. *Nanoscale Adv.* **2019**, *1*, 2645–2653. [\[CrossRef\]](#) [\[PubMed\]](#)
19. Wang, D.; Su, D. Heterogeneous nanocarbon materials for oxygen reduction reaction. *Energy Environ. Sci.* **2014**, *7*, 576–591. [\[CrossRef\]](#)
20. Li, Y.; Luo, S.; Yang, L.; Liu, C.; Chen, Y.; Meng, D. Photo-assisted synthesis of rose-like CuSe hierarchical nanostructures on TiO<sub>2</sub> nanotubes with remarkable photocatalytic performance. *Electrochim. Acta* **2014**, *83*, 394–401. [\[CrossRef\]](#)
21. Liu, C.; Sun, C.; Gao, Y.; Lan, W.; Chen, S. Improving the Electrochemical Properties of Carbon Paper as Cathodes for Microfluidic Fuel Cells by the Electrochemical Activation in Different Solutions. *ACS Omega* **2021**, *6*, 19153–19161. [\[CrossRef\]](#)
22. Zhu, W.; Zhang, X.; Yin, Y.; Qin, Y.; Zhang, J.; Wang, Q. In-situ electrochemical activation of carbon fiber paper for the highly efficient electroreduction of concentrated nitric acid. *Electrochim. Acta* **2018**, *291*, 328–334. [\[CrossRef\]](#)
23. Wang, Z.; Han, Y.; Zeng, Y.; Qie, Y.; Wang, Y.; Zheng, D.; Lu, X.; Tong, Y. Activated carbon fiber paper with exceptional capacitive performance as a robust electrode for supercapacitors. *J. Mater. Chem. A* **2016**, *4*, 5828–5833. [\[CrossRef\]](#)
24. Zhang, X.; Zhang, S.; Zhu, W.; Yin, Y.; Qin, Y.; Zhang, J.; Wang, Q. Synergetic electrochemical HNO<sub>3</sub> reduction on the activated-CFP supported nano-Pt electrodes. *J. Electroanal. Chem.* **2020**, *869*, 114182–114185. [\[CrossRef\]](#)
25. Li, L.; Tang, C.; Zheng, Y.; Xia, B.; Zhou, X.; Xu, H.; Qiao, S. Tailoring Selectivity of Electrochemical Hydrogen Peroxide Generation by Tunable Pyrrolic-Nitrogen-Carbon. *Adv. Energy Mater.* **2020**, *10*, 2000789–2000799. [\[CrossRef\]](#)
26. Fan, X.; Lu, Y.; Xu, H.; Kong, X.; Wang, J. Reversible redox reaction on the oxygen-containing functional groups of an electrochemically modified graphite electrode for the pseudo-capacitance. *J. Mater. Chem.* **2011**, *21*, 18753–18760. [\[CrossRef\]](#)
27. Singh, P.R.; Zeng, X. Size-Dependent Intercalation of Ions into Highly Oriented Pyrolytic Graphite in Ionic Liquids: An Electrochemical Atomic Force Microscopy Study. *J. Phys. Chem. C* **2011**, *115*, 17429–17439. [\[CrossRef\]](#)
28. Song, Y.; Feng, D.; Liu, T.; Li, Y.; Liu, X. Controlled partial-exfoliation of graphite foil and integration with MnO<sub>2</sub> nanosheets for electrochemical capacitors. *Nanoscale* **2015**, *7*, 3581–3587. [\[CrossRef\]](#)
29. Zheng, J.; Zhang, X.; Li, P.; Zhou, X.; Yuan, W. Microstructure effect of carbon nanofiber on electrocatalytic oxygen reduction reaction. *Catal. Today* **2008**, *131*, 270–277. [\[CrossRef\]](#)
30. Ustarroz, J.; Altantzis, T.; Hammons, J.A.; Hubin, A.; Bals, S.; Terryn, H. The Role of Nanocluster Aggregation, Coalescence, and Recrystallization in the Electrochemical Deposition of Platinum Nanostructures. *Chem. Mater.* **2014**, *26*, 2396–2406. [\[CrossRef\]](#)
31. Hu, F.; Chen, S.; Wang, C.; Yuan, R.; Yuan, D.; Wang, C. Study on the application of reduced graphene oxide and multiwall carbon nanotubes hybrid materials for simultaneous determination of catechol, hydroquinone, p-cresol and nitrite. *Anal. Chim. Acta* **2012**, *724*, 40–46. [\[CrossRef\]](#) [\[PubMed\]](#)
32. Zhang, G.; Yang, D.; Edward, S. X-ray Photoelectron Spectroscopic Analysis of Pt Nanoparticles on Highly Oriented Pyrolytic Graphite, Using Symmetric Component Line Shapes. *J. Phys. Chem. C* **2007**, *111*, 565–570. [\[CrossRef\]](#)
33. Jiajun, W.; Geping, Y.; Yuyan, S.; Sheng, Z.; Zhenbo, W.; Yunzhi, G. Effect of carbon black support corrosion on the durability of Pt/C catalyst. *J. Power Sources* **2007**, *171*, 331–339.
34. Wakisaka, M.; Suzuki, H.; Mitsui, S.; Uchida, H.; Watanabe, M. Increased oxygen coverage at Pt-Fe alloy cathode for the enhanced oxygen reduction reaction studied by EC-XPS. *J. Phys. Chem. C* **2008**, *112*, 2750–2755. [\[CrossRef\]](#)
35. Balbuena, P.B.; Altomare, D.; Vadlamani, N.; Bingi, S.; Agapito, L.A.; Seminario, J.M. Adsorption of O, OH, and H<sub>2</sub>O on Pt-based bimetallic clusters alloyed with Co, Cr, and Ni. *J. Phys. Chem. A* **2004**, *108*, 6378–6384. [\[CrossRef\]](#)
36. Robert, M.D.; Jeremy, P.M. Kinetic Model of Platinum Dissolution in PEMFCs. *J. Electrochem. Soc.* **2003**, *150*, A1523–A1527.
37. Li, R.; Guan, Q.; Wei, R.; Yang, S.; Shu, Z.; Dong, Y.; Chen, J.; Li, W. A Potential Regularity for Enhancing the Hydrogenation Properties of Ni<sub>2</sub>P. *J. Phys. Chem. C* **2015**, *119*, 2557–2565. [\[CrossRef\]](#)
38. Gatewood, D.S.; Schull, T.L.; Baturina, O.; Pietron, J.J.; Garsany, Y.; Swider-Lyons, K.E.; Ramaker, D.E. Characterization of ligand effects on water activation in triarylphosphine-stabilized Pt nanoparticle catalysts by X-ray absorption spectroscopy. *J. Phys. Chem. C* **2008**, *112*, 4961–4970. [\[CrossRef\]](#)
39. Daqin, G.; Jian, Z.; Hengyue, X.; Yu-Cheng, H.; Zhiwei, H.; Bin, C.; Yuan, Z.; Meng, N.; Xiaomin, X.; Wei, Z.; et al. A universal chemical-induced tensile strain tuning strategy to boost oxygen-evolving electrocatalysis on perovskite oxides. *Appl. Phys. Rev.* **2022**, *9*, 011422–011433.
40. Ustarroz, J.; Geboes, B.; Vanrompay, H.; Sentosun, K.; Bals, S.; Breugelmans, T.; Hubin, A. Electrodeposition of Highly Porous Pt Nanoparticles Studied by Quantitative 3D Electron Tomography: Influence of Growth Mechanisms and Potential Cycling on the Active Surface Area. *ACS Appl. Mater. Interfaces* **2017**, *9*, 16168–16177. [\[CrossRef\]](#)



41. Eiler, K.; Molmen, L.; Fast, L.; Leisner, P.; Sort, J.; Pellicer, E. Oxygen reduction reaction and proton exchange membrane fuel cell performance of pulse electrodeposited Pt-Ni and Pt-Ni-Mo(O) nanoparticles. *Mater. Today Energy* **2022**, *27*, 101023–101034. [[CrossRef](#)]
42. Topalov, A.A.; Zeradjanin, A.R.; Cherevko, S.; Mayrhofer, K.J.J. The impact of dissolved reactive gases on platinum dissolution in acidic media. *Electrochem. Commun.* **2014**, *40*, 49–53. [[CrossRef](#)]

**Disclaimer/Publisher’s Note:** The statements, opinions and data contained in all publications are solely those of the individual author(s) and contributor(s) and not of MDPI and/or the editor(s). MDPI and/or the editor(s) disclaim responsibility for any injury to people or property resulting from any ideas, methods, instructions or products referred to in the content.